*Publications of the Astronomical Society of Australia* (2025), **42**, e144, 12 pages
doi:10.1017/pasa.2025.10105

CAMBRIDGE UNIVERSITY PRESS

## Research Article

# Possible detection of HFQPOs associated with 'unknown' variability class of GRS 1915+105

Seshadri Majumder[1], Santabrata Das[1] and Anuj Nandi[2]

[1]Indian Institute of Technology Guwahati, Guwahati, India and [2]ISITE Campus, U. R. Rao Satellite Centre, Marathahalli, Bangalore, India

**Abstract**

We present a comprehensive spectro-temporal analysis of GRS 1915 + 105 observed with *AstroSat* during June, 2017. A detailed study of the temporal properties reveals the appearance of an 'unknown' variability class ($\tau$) during $\rho \rightarrow \kappa$ class transition of the source. This new 'unknown' class ($\tau$) is characterised by the irregular repetition of low count 'dips' along with the adjacent 'flare' like features in between two successive steady count rate durations, resulting in uniform '*C*' shaped distribution in the colour-colour diagram. A detailed comparative study of the variability properties between the $\tau$ class and other known variability classes of GRS 1915 + 105 indicates it as a distinct variability class of the source. Further, we find evidence of the presence of possible HFQPO features at ∼71 Hz with quality factor ∼13, rms amplitude ∼4.69%, and significance $3\sigma$, respectively. In addition, a harmonic-like feature at ∼152 Hz is also seen with quality factor ∼21, rms amplitude ∼5.75%, and significance $\sim 4.7\sigma$. The energy-dependent power spectral study reveals that the fundamental HFQPO and its harmonic are present in 3–15 keV and 3–6 keV energy ranges, respectively. Moreover, the wide-band (0.7–50 keV) spectral modelling comprising of thermal Comptonization component indicates the presence of a cool ($kT_e \sim 1.7$ keV) and optically thick (optical depth ∼14) Comptonizing 'corona', which seems to be responsible in regulating the HFQPO features in GRS 1915+105. Finally, we find the bolometric luminosity ($L_{bol}$) to be about 42%$L_{Edd}$ within 1–100 keV, indicating the sub-Eddington accretion regime of the source.

**Keywords:** Accretion, accretion disks; black hole physics; X-rays: binaries; stars: individual (GRS 1915+105)

(Received 16 December 2024; revised 22 September 2025; accepted 29 September 2025)

## 1. Introduction

GRS 1915+105, being an enigmatic Galactic black hole X-ray binary source (BH-XRB), exhibits exceptionally complex variability properties (Greiner, Morgan, & Remillard 1996; Paul et al. 1997; Taam, Chen, & Swank 1997; Paul et al. 1998a; Paul et al. 1998b; Paul et al. 1998c; Yadav et al. 1999; Morgan et al. 1999; Muno, Morgan, & Remillard 1999; Belloni et al. 2000; Naik et al. 2002; Chakrabarti et al. 2004; Rodriguez et al. 2004; Belloni & Altamirano 2013b; Weng et al. 2018; Zhang et al. 2022; Athulya et al. 2022; Majumder et al. 2022; Athulya & Nandi 2023) in different time scales ranging from seconds to hours. The rich variability properties of GRS 1915+105 render this source a unique astrophysical laboratory to study the accretion dynamics around black holes. The distinct variability pattern observed in the light curves and the corresponding Color-Color Diagrams (CCDs) manifest 15 unique classes (Belloni et al. 2000; Klein-Wolt et al. 2002; Hannikainen et al. 2005; Pahari & Pal 2009) during *RXTE* era. So far, eight confirmed variability classes, namely θ, χ, ω, δ, β, ρ, κ, and γ of GRS 1915+105, are observed with *AstroSat* during 2016–2022 (Athulya et al. 2022; Majumder et al. 2022; Athulya & Nandi 2023). Interestingly, an intermediate variability state, characterised by unstructured broad patterns in the light curve are also observed with *AstroSat* during the transition from quiet χ to structured ρ class transition (Rawat et al. 2019; Athulya et al. 2022).

Meanwhile, several attempts have been made to explain the rich variability properties and transition between different classes of GRS 1915 + 105. For instance, Greiner et al. (1996) argued for an accretion disc instability mechanism to be responsible for the quasi-periodic variation in the X-ray light curves of varying duration and repetition timescales. Further, a disc-corona configuration was attributed to the rapid regular/irregular variabilities of the source (Taam et al. 1997; Vilhu & Nevalainen 1998). Interestingly, Nandi, Manickam, & Chakrabarti (2000) proposed that the variability classes of GRS 1915 + 105 can be classified into four different types, which are closely connected to the 'softness ratio' diagram associated with the Kepleran and sub-Keplerian accretion flows. In addition, Chakrabarti & Nandi (2000) suggested that the transition between three fundamental accretion states of GRS 1915 + 105 results in the observed variability patterns. Subsequently, the feedback of the failed disc winds to the accretion flow is conjectured to be associated with the well-known 'On' state of the source, possibly responsible for the flickering in light curves of several classes (Nandi et al. 2001). Further, Janiuk, Czerny, & Siemiginowska (2002) argued that the lack of direct transition from the canonical 'state *C*' to 'state *B*' in the CCDs of GRS 1915 + 105 can be explained considering the time evolution of a viscous disc driven by the instabilities at the innermost region. However, Chakrabarti et al. (2005) suggests that the transition between variability classes on a timescale much shorter than the viscous time is attributed to the change in the accretion rate

**Corresponding author:** Seshadri Majumder, Email: smajumder@iitg.ac.in.

**Cite this article:** Majumder S, Das S and Nandi A. (2025) Possible detection of HFQPOs associated with 'unknown' variability class of GRS 1915+105. *Publications of the Astronomical Society of Australia* **42**, e144, 1–12. https://doi.org/10.1017/pasa.2025.10105

© The Author(s), 2025. Published by Cambridge University Press on behalf of Astronomical Society of Australia. This is an Open Access article, distributed under the terms of the Creative Commons Attribution licence (https://creativecommons.org/licenses/by/4.0/), which permits unrestricted re-use, distribution and reproduction, provided the original article is properly cited.

of the sub-Keplerian flow. This further corroborates the presence of nearly freely falling low angular momentum accretion flow as the source of rapid variability in the count rates during the transitions. In addition, Neilsen, Remillard, & Lee (2011) proposed that the radiation pressure-driven mass loss from the inner disc at near Eddington luminosity is sufficient enough to explain the oscillation in accretion rate, resulting in the hard pulses seen in the ρ class light curve of 'heartbeat' state in GRS 1915 + 105. However, detection of ρ class with *AstroSat* in the sub-Eddington accretion state further challenges the proposed models to explain the complex nature of the variability classes (Athulya et al. 2022).

GRS 1915+105 occasionally exhibits the High-Frequency Quasi-periodic Oscillations (HFQPOs) feature, which is believed to be one of the most powerful diagnostic tools to probe the effect of strong gravity in the vicinity of black holes. Indeed, several other BH-XRBs, namely XTE J1550 − 564, GRO J1655 − 40, IGR J17091 − 3624, and H 1743 − 322 display HFQPOs in the frequency range of ∼65 − 450 Hz (Remillard et al. 2006). Among these sources, GRS 1915+105 particularly draws considerable attention because of its stable HFQPOs at ∼70 Hz, which is observed on multiple occasions by both *RXTE* (Strohmayer 2001a; Remillard et al. 2002; Belloni & Altamirano 2013b, and references therein) and *AstroSat* (Sreehari et al. 2020; Majumder et al. 2022; Majumder, Dutta, & Nandi 2024; Majumder, Dutta, & Nandi 2025; Harikesh et al. 2025, and references therein). Interestingly, some of the 'softer' variability classes of GRS 1915+105, such as δ, κ, ω, γ, μ, ρ, and ν, are found to exhibit the HFQPO features (Belloni & Altamirano 2013b; Majumder et al. 2022), which are attributed to the modulation of inner 'Comptonizing corona' (Sreehari et al. 2020; Majumder et al. 2022). Moreover, simultaneous detection of additional features at ∼34 Hz and 41 Hz along with the 70 Hz HFQPO are also reported occasionally (Strohmayer 2001b; Belloni & Altamirano 2013a).

Furthermore, the phase/time lag properties associated with the HFQPOs of GRS 1915+105 are also extensively studied with both *RXTE* and *AstroSat*. For example, hard phase lag is attributed to the HFQPO feature at 67 Hz, whereas soft lag is seen at 34 Hz with *RXTE* observations (Méndez et al. 2013). Although, energy dependent soft time lags of maximum ∼3 ms duration have been observed at HFQPO (∼70 Hz) in different variability classes (δ, ω, κ, γ) of GRS 1915+105 with *AstroSat* (Majumder et al. 2024). This is further elucidated by the reflection of hard photons in the cooler accretion disc, giving rise to the observed soft time delay (Majumder et al. 2024).

Intriguingly, GRS 1915+105 remained active (Balakrishnan et al. 2021; Motta et al. 2021; Athulya et al. 2022; Parrinello et al. 2023) for last few decades since its discovery by *WATCH* onbroad *GRANAT* in 1992 (Castro-Tirado, Brandt, & Lund 1992) before its quiescence phase from 2018, followed by sporadic re-brightenings in 2019 (Athulya & Nandi 2023). The source is continuously monitored by *AstroSat* from 2016 onwards providing quality observations. Therefore, it becomes immensely appealing to study the spectro-temporal characteristics over different variability classes of the source. Indeed, a comprehensive wide-band spectro-temporal study is carried out by Athulya et al. (2022) to probe the evolution in the accretion dynamics of the source. Further, a multimission study of the 'obscured' phase of GRS 1915 + 105 results in the detection of several emission and absorption spectral lines along with mHz QPOs in the power spectra (Athulya & Nandi 2023).

In this work, we present the results of an in-depth spectro-temporal study of two *AstroSat* observations of GRS 1915 + 105 during June, 2017. While doing so, we carry out a detailed temporal study and find the presence of an 'unknown' variability class than the previously known 15 classes of the source. In addition, we find the evidence of possible HFQPOs at 71 Hz and its harmonic-like feature at ∼152 Hz. Further, the energy dependent characteristics of the observed HFQPO signatures are also examined. Subsequently, we study the wide-band (0.7–50 keV) spectral properties of the source and put efforts into explaining the anticipated origin of the possible HFQPO features observed in GRS 1915 + 105 during the 'unknown' variability class.

The paper is organised as follows. In Section 2, we mention the details of the selected observations and describe the data reduction procedure. In Sections 3 and 4, we present the in-depth temporal and spectral analysis with results, respectively. We discuss the obtained results in Section 5, and finally, conclude in Section 6.

## 2. Observation and data reduction

In the present work, we analyse two Guaranteed Time (GT) observations of GRS 1915+105 during June 2017 with *SXT* and *LAXPC* onboard *AstroSat* (Agrawal 2006; Singh et al. 2014; Agrawal et al. 2017). Three more adjacent observations available with *AstroSat* and *NuSTAR* during May−July, 2017 are also analysed. Additionally, we analyse three *RXTE/PCA* observations (RX0−RX2) in our study, which are available in the `HEASARC` archive.[a] The details of all these observations are tabulated in Table 1 along with Epoch numbers. The Epochs of these observations are marked using vertical lines in the MAXI/GSC light curve (Figure 1).

We extract *LAXPC* (Antia et al. 2017) level-1 data in event analysis mode, available in *AstroSat* public archive[b] using the standard data reduction software `LaxpcSoftv3.4.4`.[c] The details of *LAXPC* data extraction procedure and analysis methods are mentioned in Sreehari et al. (2019, 2020), Majumder et al. (2022). It is worth mentioning that, due to the constraints of Earth occultation and passage of the satellite in the region of South Atlantic Anomaly (SAA), continuous observation is not possible with *AstroSat*. Subsequently, the data corresponding to a given observation of *AstroSat/LAXPC* are generally divided into multiple Good Time Interval (GTI) segments of the observation time using the analysis software. For example, the entire data of AS1 observation contains 4 GTI segments (1*a*, 1*b*, 1*c*, and 1*d*) (see Table 1), which are distributed over 4 orbits of observation. Further, we mention that the timing analyses including the study of variability properties and power density spectra are carried out for such individual segments excluding the data gaps, whereas the spectral analysis is performed considering the entire observation data of AS1 and AS2.

We utilise both *LAXPC10* and *LAXPC20* data for the timing analyses, whereas only *LAXPC20* data are used in the spectral study following Antia et al. (2021), Majumder et al. (2022). Note that, the data from the top layer of the detectors and that corresponds to the single events are considered for the analysis. Accordingly, we generate the source and background spectra along with instrument response files for *LAXPC20* following Antia et al. (2017). We analyse the *SXT* (Singh et al. 2016, 2017) data following the guidelines provided by the *SXT* instrument team.[d]

[a] https://heasarc.gsfc.nasa.gov/db-perl/W3Browse/w3browse.pl.
[b] https://webapps.issdc.gov.in/astro_archive/archive/Home.jsp.
[c] http://www.tifr.res.in/astrosat_laxpc/LaxpcSoft.html.
[d] https://www.tifr.res.in/astrosat_sxt/index.html.

https://doi.org/10.1017/pasa.2025.10105 Published online by Cambridge University Press

**Table 1.** Observation details of GRS 1915 + 105 observed by *AstroSat* and *NuSTAR* during June, 2017. Column 1, 2, 4, 5, and 6 are for ObsID, Epoch, Orbit number, MJD and exposure time. In column 3, 'Seg.' denotes the light curve segments for Epochs AS1 and AS2. The mean detected ($r_{det}$) and incident ($r_{in}$) count rates, along with the mean hardness ratios (HRs) over the entire exposures for each variability class, are tabulated. HR1_var, HR2_var, and $r_{det}$_var are the fractional variabilities of the respective quantities. In column 14–15, the variability classes and the presence of Low/High-frequency QPO features in respective observations are given. See the text for details.

| ObsID | Epoch | Seg. | Orbit | MJD (Start) | Effective Exposure (ks) | $r_{det}$ (cts/s) | $r_{in}$ (cts/s) | HR1 (B/A)* | HR2 (C/A)* | HR1_var (%) | HR2_var (%) | $r_{det}$_var (%) | Class | LF/HF QPO |
|---|---|---|---|---|---|---|---|---|---|---|---|---|---|---|
| 10408-01-30-00 | RX0 | 2 | – | 50313.31 | 3.4 | 16 919 | – | 0.68 | 0.09 | 2 | 7 | 7 | $\chi_3$ | LF |
| 20402-01-33-00 | RX1 | 2 | – | 50617.61 | 3.3 | 14 676 | – | 1.14 | 0.11 | 24 | 27 | 60 | κ | LF |
| 20402-01-53-01 | RX2 | 1 | – | 50757.21 | 3.2 | 21 288 | – | 1.02 | 0.08 | 17 | 21 | 27 | μ | – |
| G07_046T01_9000001236 | AS0 | – | 8 876 | 57892.74 | 3.63 | 1 292 | 1 328 | 0.61 | 0.09 | 13 | 28 | 42 | ρ | LF |
| G07_028T01_9000001272 | AS1 | 1*a* | 9 127 | 57909.77 | 2.43 | 2 156 | 2 259 | 0.62 | 0.04 | 16 | 37 | 60 | unknown | – |
| | | 1*b* | 9 127–9 128 | 57909.83 | 3.36 | 2 236 | 2 348 | 0.62 | 0.04 | 16 | 44 | 62 | unknown | HF |
| | | 1*c* | 9130 | 57909.89 | 2.95 | 2 235 | 2 346 | 0.62 | 0.04 | 17 | 49 | 72 | unknown | – |
| | | 1*d* | 9 130–9 131 | 57909.98 | 0.94 | 2 133 | 2 235 | 0.60 | 0.04 | 15 | 30 | 48 | unknown | – |
| G07_046T01_9000001274 | AS2 | 2*a* | 9 131–9 136 | 57909.99 | 6.53 | 2 135 | 2 236 | 0.61 | 0.04 | 15 | 29 | 47 | unknown | – |
| | | 2*b* | 9 136–9 139 | 57910.43 | 9.03 | 2 167 | 2 272 | 0.60 | 0.04 | 14 | 31 | 45 | unknown | HF |
| | NU1 | – | – | 57928.67 | 18.4 | 572 | – | 0.78 | 0.02 | 7 | 31 | 4 | δ | – |
| G07_028T01_9000001370 | AS3 | – | 9 629 | 57943.69 | 0.98 | 2 814 | 2 993 | 0.76 | 0.04 | 21 | 43 | 47 | κ | – |

*A, B, and C are the count rates in 3–6, 6–15, and 15–60 keV energy ranges, respectively.

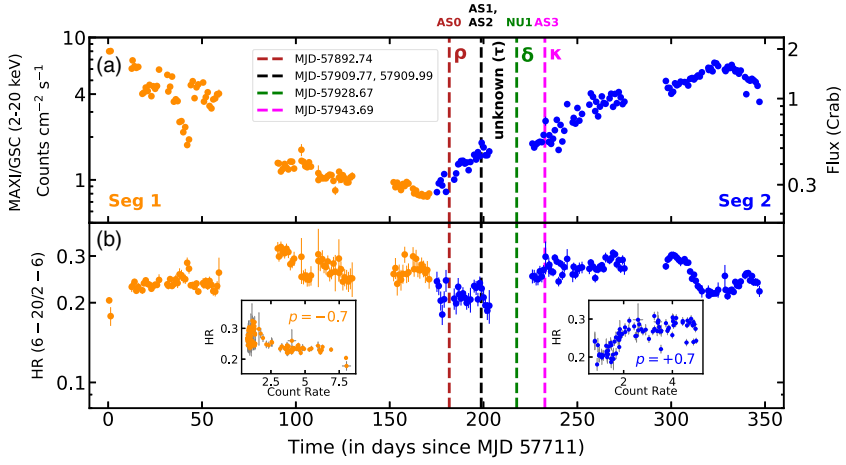



**Figure 1.** (a) *MAXI/GSC* daily light curve in the energy band of 2–20 keV in flux units of counts cm$^{-2}$ s$^{-1}$. (b) The variation of the hardness ratio defined as the ratio of 6–20 to 2–6 keV count rates with the time of observation. In panel (b), the insets show the variation of the hardness ratio with the corresponding count rates, indicated by distinct colours (orange and blue). *p* denotes the Pearson correlation coefficient between the count rate and hardness ratio distributions. Different coloured vertical dashed lines represent the Epochs of observations with *AstroSat* and *NuSTAR*, respectively. See the text for details.

The *SXT* light curves, spectra, and ancillary response files are extracted using `XSELECT V2.5b` from a 12 arcmin circular source region using the level-2 cleaned event files available at ISSDC[e] data archive.

The *NuSTAR* data analysis is carried out using the latest mission specific software available at `HEASOFT V6.32.1`.[f] The task *nupipeline* is used to generate the cleaned event file from the data of both *FPMA* and *FPMB* instruments of *NuSTAR*. Following Nathan et al. (2022), a circular region of 50 arcsec at the source position and away from the source is considered to obtain the source and background products, respectively. We use the *nuproduct* task to generate the source and background light curves.

[e]https://webapps.issdc.gov.in/astro_archive/archive/Home.jsp.
[f]https://heasarc.gsfc.nasa.gov/docs/software/heasoft/.

*RXTE/PCA* data available both in Binned and Event mode are analysed for timing studies. We extract the light curves of different time resolutions across various energy bands using the `saextrct` and `seextrct` tasks available in `FTOOLS` for the Binned mode and Event mode data, respectively (see Nandi et al. 2012 for details). Note that during the observation of RX0 – RX2 Epochs, all five PCUs of *RXTE/PCA* were on.

## 3. Temporal analysis and results

### 3.1. MAXI/GSC monitoring of GRS 1915+105

We study the evolution of the source GRS 1915 + 105 with daily MAXI/GSC monitoring. In Figure 1a, we present the light curve in 2–20 keV energy range during MJD 57711 – 58061. In Figure 1b,

https://doi.org/10.1017/pasa.2025.10105 Published online by Cambridge University Press

we show the variation of hardness ratio (HR) defined as the ratio of counts in 6–20 keV and 2–6 keV energy bands. The dashed vertical lines in brown, black, green, and magenta denote the Epochs corresponding to *AstroSat* and *NuSTAR* observations under consideration. Further, we carry out a correlation study between HR and count rates for two distinct regions of the MAXI/GSC light curves, represented by orange (Seg 1) and blue (Seg 2) colours in Figure 1. The variation of HR against the count rates for each of these two segments is shown in the insets of Figure 1b. While computing the Pearson correlation coefficient ($p$) of these distributions, we consider all the data points in Seg 1, whereas count rates exceeding 5 counts cm$^{-2}$ s$^{-1}$ are excluded for Seg 2. With this, we find a strong negative (positive) correlation between HR and count rate for Seg 1 (Seg 2) with $p = -0.7\,(+0.7)$ for one-tailed chance probability of $3.1 \times 10^{-16}$ ($5.1 \times 10^{-15}$).

Moreover, we note that the *AstroSat* observations considered in this study fall within the Seg 2 region. This suggests that, during this period, the source was exhibiting 'softer' spectral characteristics with a ∼2.5 times increase in the count rate and a marginal variation in the HR. The detection of 'softer' variability classes ('unknown', δ, and κ) during this period further supports the softening behavior of the source. At the initial phase of Seg 2 the MAXI/GSC count rate was $\lesssim 1$ counts cm$^{-2}$ s$^{-1}$, during which ρ class variability characterised by quasi-periodic flares with relatively harder characteristics in the CCD (see Belloni et al. 2000) was detected. It is important to note that the canonical χ class variability of harder spectral characteristics in GRS 1915 + 105 is generally associated with the less variable quiescent state C, often persisting over longer timescales ranging from hours to months (Belloni et al. 2000). In contrast, the $\phi$ class, which resembles a typical soft state variability pattern, is seen to be connected with the outbursting state A of the source (Belloni et al. 2000). Notably, the 'softer' variability classes ('unknown', δ, and κ) remain in between these two and correspond to rapid transitions between the outbursting states and the short-lived quiescent state C on much smaller times scales of few tens of seconds.

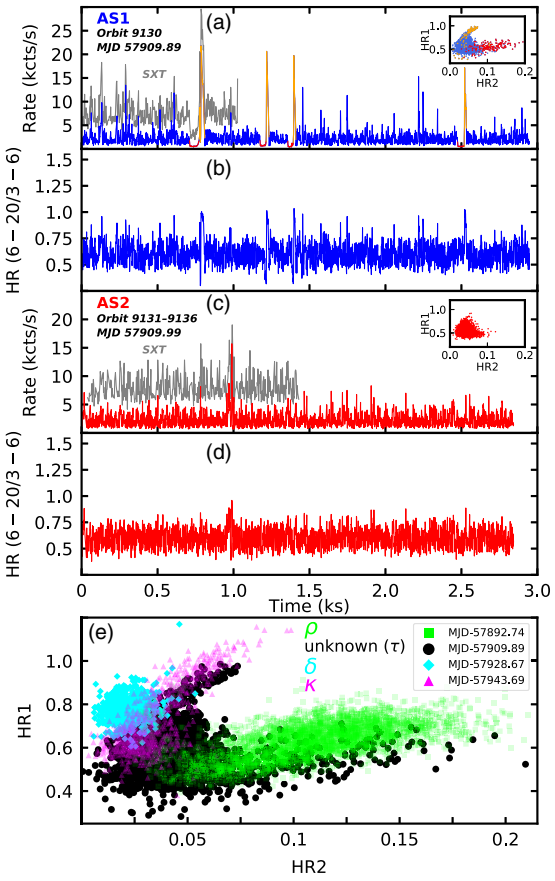



**Figure 2.** Background subtracted and dead-time corrected 1 s binned light curves (*LAXPC* in 3–60 keV) of GRS 1915+105 observed with *AstroSat* during Epoch AS1 (a) and AS2 (c), respectively. The *SXT* light curves of AS1 and AS2, simultaneous with *LAXPC* is shown with grey colour. The CCD of the same observations are shown at the top right insets, respectively. The variation of the corresponding hardness ratios are shown in panel (b) and (d). The comparison of CCDs in different variability classes under consideration is shown in panel (e). See text for details.

### 3.2. Temporal variability

We generate 1 s binned background subtracted *LAXPC10* and *LAXPC20* combined light curves in 3–60 keV energy range to investigate the variability properties of the source. The dead-time corrected average incident and detected count rates (Sreehari et al. 2020, and references therein) estimated in 3–60 keV energy range are given in Table 1. We generate the CCDs of each observation by defining the soft and hard colours as HR1= $B/A$ and HR2= $C/A$, where $A$, $B$, and $C$ are the count rates in 3–6, 6–15, and 15–60 keV energy bands, respectively (Sreehari et al. 2019, 2020). Similarly, the CCD of *NuSTAR* observation is calculated considering same energy bands. The average values of $HR1$ and $HR2$ for each observation are listed in Table 1. Further, we compute the fractional variability amplitude in detected count rate and HR values following Vaughan et al. (2003) and tabulate in Table 1. We present the light curves (*SXT* in grey, and *LAXPC* in blue and red) of AS1 and AS2 Epochs in Figure 2a and c along with the CCDs at top right insets. The variation of hardness ratio (HR= $D/A$) corresponding to AS1 and AS2 is depicted in Figure 2b and d, respectively, where $D$ being the count rates in 6–20 keV energy band.

Investigation of the variability patterns observed in the *LAXPC* light curve of AS1 reveals the appearance of several irregular 'dips' (low counts) of maximum ∼60 s duration (Figure 2a) between two consecutive 'non-dip' (steady counts) segments. In addition, a 'flare' like feature is also seen immediately after the 'dip'. However, Epoch AS2 exhibits almost steady light curves (Figure 2c) similar to the 'non-dip' duration of AS1. The patten of the CCD of AS2 (Figure 2c) resembles with that of AS1 ('C' shape pattern, see Figure 2a) without its two elongated branches. Further, we investigated the variability properties of AS1 and AS2 observation across different energy bands. For this, in Figure 3, we present the light curves of AS1 and AS2 observations in 3–6, 6–15, and 15–60 keV energy bands, focusing on the time interval (0.6–1.5 ks) during which the repetitive dip and spike-like features are observed (see Figure 2). Interestingly, we find that the overall structured variability pattern remains broadly similar across all energy bands, with only the count rate varying between them. More specifically, we observe that the low-count 'dip' features in the light curve are most prominent and pronounced in the 3–6 and 6–15 keV energy bands, but they disappear in the 15–60 keV band. In contrast, the characteristics of the spike-like features remain similar across all energy bands. In addition, during the AS2 observation, the structured variability shows marginal differences in different energy bands.

The observed variability pattern seems to be different from the known 15 variability classes of GRS 1915+105. Indeed, the overall

https://doi.org/10.1017/pasa.2025.10105 Published online by Cambridge University Press

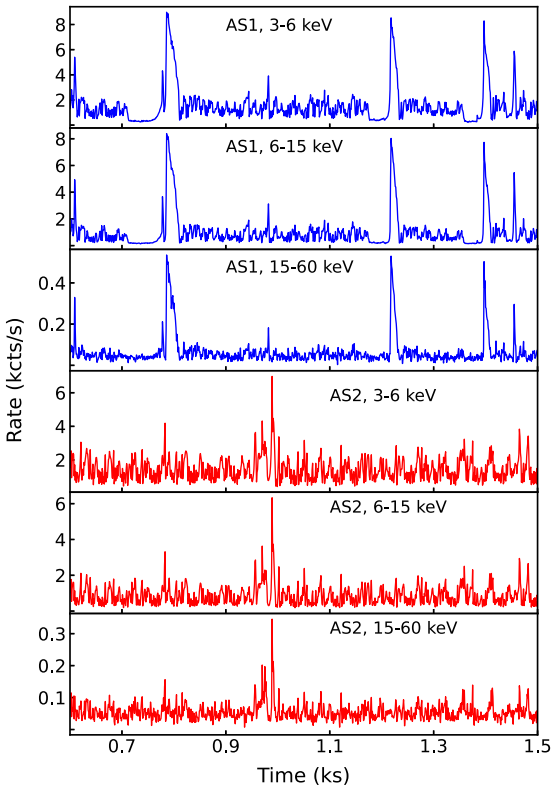



**Figure 3.** Light curves from the AS1 and AS2 observations in the 3–6, 6–15, and 15–60 keV energy ranges are shown in the top, middle, and bottom panels, respectively. These segments correspond to the 0.6–1.5 ks interval of the full light curves shown in Figure 2, highlighting the structured variability. See text for details.

shape of the CCD in AS1 is coarsely similar to the λ class, however, the variability pattern and the duration of 'dip' and 'non-dip' segments are distinctly different from the λ and κ classes. Further, the 'flare' like features observed just after the 'dips' in AS1 seem to be similar to ρ class (Belloni et al. 2000; Athulya et al. 2022). In a preceding observation with *AstroSat* (AS0 in Figure 1, see Table 1) 16 days before AS1, the source was in ρ class (Athulya et al. 2022). In addition, the source was observed in κ class (Epoch AS3 in Figure 1, see Table 1) after 33 days of AS2. Interestingly, the *NuSTAR* observation (NU1 in Figure 1, see Table 1) which is 15 days prior to AS3 shows δ class variability. All the above findings clearly indicate that the source exhibits multiple class transitions within a months timescale during Epoch AS0 to AS3. Therefore, we infer that possibly GRS 1915 + 105 went through an 'unknown' variability class rather than the previously known 15 distinct classes. However, we also note that due to the lack of continuous observations of the source, we are unable to track all possible class transitions that might have occurred on timescales of hours to days, as is typically seen for GRS 1915+105 (Chakrabarti et al. 2005).

In Figure 2e, we compare the CCDs generated from Epochs AS0, AS1, NU1, and AS3 (Table 1). It is evident that the source underwent transition from ρ to κ class via an 'unknown' and δ class variabilities. A detailed investigation of the CCDs indicates that the 'harder' tail (black filled circles with HR1 $\lesssim 0.6$ and HR2 $\gtrsim 0.07$) and the 'softer' branch (HR1 $\gtrsim 0.6$ and HR2 $\lesssim 0.07$) of AS1 overlap with the distributions of a ρ (filled green squares) and κ (filled magenta triangles) classes, respectively. We observe that δ class (filled cyan diamonds), generally 'softer' in nature, appears in between AS0 and AS3, and it makes the 'unknown' class more complex as the CCD shows the mixed properties of both ρ and κ classes. This further corroborates the appearance of an 'unknown' variability class which is characterised by the irregular soft 'dips' along with 'flare' like spikes in the light curve between two consecutive steady count rates.

### 3.3. Comparison with $\chi_3$, κ, and μ classes

In this section, we perform a comparative study between the variability properties of the 'unknown' class (AS1 and AS2) and the canonical $\chi_3$, κ, and μ classes observed with *RXTE/PCA* (see Table 1). In doing so, we present 1 s time binned light curves of the $\chi_3$, κ, and μ classes in Figure 4 with CCDs at the insets, obtained from the *RXTE/PCA* data in 3–60 keV energy band. Note that, to compare with AS1 and AS2 observations, we obtain the CCDs of $\chi_3$, κ, and μ classes using the definition of soft colour and hard colour as $HR1 = B/A$ and $HR2 = C/A$, respectively, where $A$, $B$, and $C$ represent the light curves in 3–6, 6–15, and 15–60 keV energy bands, respectively. It is important to note that the observed structured variability pattern in the light curve and the shape of the CCD for a given class largely depend on both effective area of the instruments used and, to some extent, the overall flux level of the source. For instance, the *AstroSat/LAXPC* observations were conducted at a relatively lower source intensity of ∼555 mCrab and with a much larger effective area beyond ∼10 keV (Beri et al. 2019). In contrast, the *RXTE/PCA* observations were performed during a much brighter phase of the source (∼1.2 Crab). Because of that, despite the sharply declining effective area of *RXTE/PCA* beyond ∼10 keV, the count rates at higher energies may increase significantly, thereby altering the hardness ratios. Keeping these limitations in mind, in this section, we focus solely on a qualitative comparison between the CCDs of different classes observed with *RXTE/PCA* and the 'unknown' variability class observed with *AstroSat/LAXPC*.

In Figures 2 and 4, we observe that the structured variability in the 'unknown' class remains different from the individual variability patterns of $\chi_3$ and μ classes mainly due to the appearance of irregular small duration dips followed by high count spikes in AS1. Interestingly, these dip features appear somewhat similar to the low-count dips of varying durations observed in the κ class (see Figure 4). However, we find that the typical duration of these dips is about ∼60 s in AS1, whereas it varies between ∼50–90 s in the κ class. Moreover, the fractional noise amplitudes (defined as the standard deviation normalised by the mean count rate) of these dip intervals are found to be ∼9.3% and ∼15.2–17.4% for the 'unknown' and κ variability classes observed with *AstroSat* and *RXTE*, respectively. This suggests that although an apparent similarity exists between the dip segments of the canonical κ class and those of the 'unknown' variability class observed during AS1, the intrinsic noise amplitude is nearly twice as high in the case of the κ class, indicating different underlying variability processes. Moreover, we also find that the noise amplitudes of the dip segments in AS1 are nearly twice that of the corresponding Poisson noise in these intervals, implying the presence of intrinsic variability during the dip durations beyond random statistical fluctuations. Given the similarity between the small-amplitude spikes observed during the steady interval of the 'unknown' class (AS2) and those seen in the $\chi_3$ variability class, we compare the Poisson noise-subtracted intrinsic fractional variability amplitude

https://doi.org/10.1017/pasa.2025.10105 Published online by Cambridge University Press

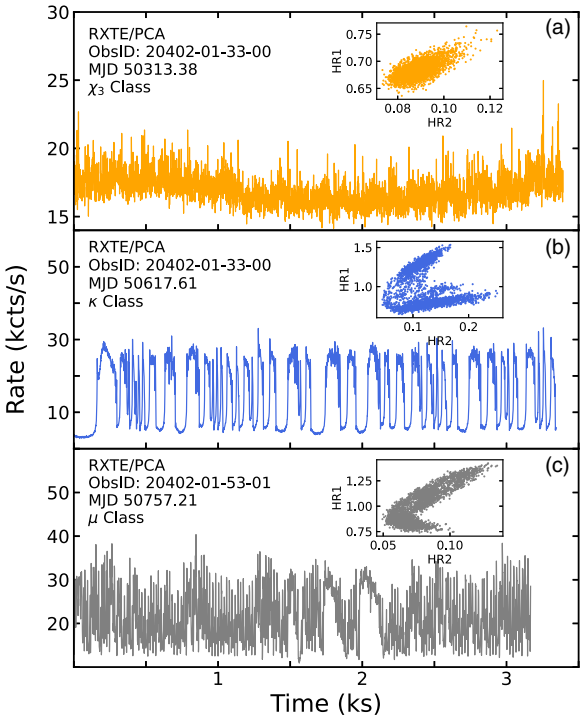



**Figure 4.** *RXTE/PCA* light curves of 1 s time bin of the source GRS 1915 + 105 in 3–60 keV energy range corresponding to $\chi_3$, κ, and μ variability classes. The CCDs of the respective classes are presented in the insets of each panel. See text for details.

($F_{\rm var}$) for these two cases. For this, we compute $F_{\rm var}$ following Vaughan et al. (2003) for both $\chi_3$ class and AS2 observation. We find that $F_{\rm var} \sim 7\%$ for $\chi_3$ class, whereas it increases significantly to ∼45–47% during the AS2 observation. This indicates that the small-amplitude spikes and fluctuations observed in the steady interval of the 'unknown' variability class are intrinsically different from the variability characteristics of the $\chi_3$ class.

Further, we find that the distribution of *HR*1 and *HR*2 in the CCD (see Figure 2c) of AS1 observation remains completely different from the canonical $\chi_3$ class but resemble with that of κ and μ class to some extent (see Figure 4). However, the upper and lower branches of the μ class CCD remain asymmetric, whereas a more extended lower branch towards higher *HR*2 values is observed for the AS1 observation.

Furthermore, we compare the characteristics of the present 'unknown' class in context of the canonical states of GRS 1915+105 proposed by Belloni et al. (2000). We note that, Belloni et al. (2000) identified three basic spectral states while classifying the variability properties of GRS 1915+105. Among these, state C and state B correspond to the quiescent and outburst states, respectively. More specifically, state C is associated with low flux and is harder in nature, typically located towards the higher HR2 region of the CCD. In contrast, state B is characterised by high flux, higher HR1, and lower HR2 values. In addition to these, another state known as state A is observed during transitions between states B and C. In general, state A exhibits low flux but softer spectral colours and is typically located in the lower-left region of the CCD.

It is important to mention that the λ and κ, basic classes of GRS 1915 + 105 (Belloni et al. 2000), exhibit low-flux dips associated with the quiescent state C and repeated high-count episodes corresponding to the outburst state B (Belloni et al. 2000). Typically, the low-count dips of varying durations remain located along the lower branch of the CCD in these two classes. Similarly, we observe that the low flux dips of the 'unknown' class during AS1 form the harder branch of the CCD (see inset in Figure 2a) and resemble the quiescent state C of GRS 1915 + 105, as proposed by Belloni et al. (2000). On the other hand, high count spikes generally reside in the higher HR1 region of the CCD, indicating the possible presence of the outburst state B. However, we find the presence of a cluster of points in the CCD corresponding to steady durations characterised by small-amplitude spikes in the light curve of AS1 (see inset in Figure 2a). This region of the CCD, which exhibits softer spectral characteristics and low flux, broadly resembles state A, albeit with a much greater spread. Typically, state A appears for short durations in the λ and κ classes and therefore contributes only marginally to the CCD (Belloni et al. 2000). Nevertheless, in the present case, the irregular and structured variability observed in AS1 and AS2 observation makes it more challenging to confirm the presence of state A.

### 3.4. Power density spectra

We generate 1 ms resolution light curves with the combined data from both *LAXPC10* and *LAXPC20* in 3–60 keV energy range. This allows us to examine the power spectral properties in the wide-band frequency range of 0.01–500 Hz. Following Sreehari et al. (2020), Majumder et al. (2022), we obtain the power density spectra (PDS) for all segments of Epoch AS1 and AS2. In particular, we consider 32 768 bins per interval for generating individual PDS that are again averaged out to obtain the resultant PDS of each segment of observations. Note that, for a continuous data of exposure $T_{\rm exp}$ and time resolution $\Delta t$, the total number of individual PDS available for averaging becomes $T_{\rm exp}/32\,768\Delta t$. Thus, approximately 104 and 274 number of PDS are averaged out to obtain the resultant PDS for AS1($1b$) and AS2($2b$) observations, respectively. While doing this, if a light curve duration is found to be longer than a multiple of 32 768 bins, the excess data towards the end is truncated. This procedure is followed to adopt the computational efficiency of the Fast Fourier Transform (FFT) algorithm and to maintain consistency across different intervals, producing individual PDS of uniform frequency grids (van der Klis 1988; Uttley et al. 2014). Finally, a geometric binning factor of 1.03 is chosen to rebin the PDS in the frequency space. We mention that the errors in power are estimated from the standard deviation of power values across independent frequency bins. Further, we note that because of the geometrical rebinning, the power values within a bin are averaged and accordingly, the propagated errors are expected to introduce correlations between adjacent bins of overlapping frequency intervals. Note that, the dead-time correction of the light curves is implemented during the PDS generation following Agrawal et al. (2018), Sreehari et al. (2019, 2020). Accordingly, dead-time affected Poisson noise level is subtracted from the PDS in Leahy normalisation (Leahy et al. 1983) and the corresponding effects on rms amplitude are also corrected following Zhang et al. (1995), Sreehari et al. (2019); Sreehari et al. (2020) to obtain the PDS in the rms space.

Each PDS in rms space is modelled in `XSPEC V12.13.1` using a `constant` and `Lorentzian` functions. The `Lorentzian` function inside `XSPEC` reads as,

$$L(\nu) = \frac{K}{2\pi} \frac{\Delta}{(\nu - \nu_{\rm c})^2 + (\Delta/2)^2}, \quad (1)$$

https://doi.org/10.1017/pasa.2025.10105 Published online by Cambridge University Press

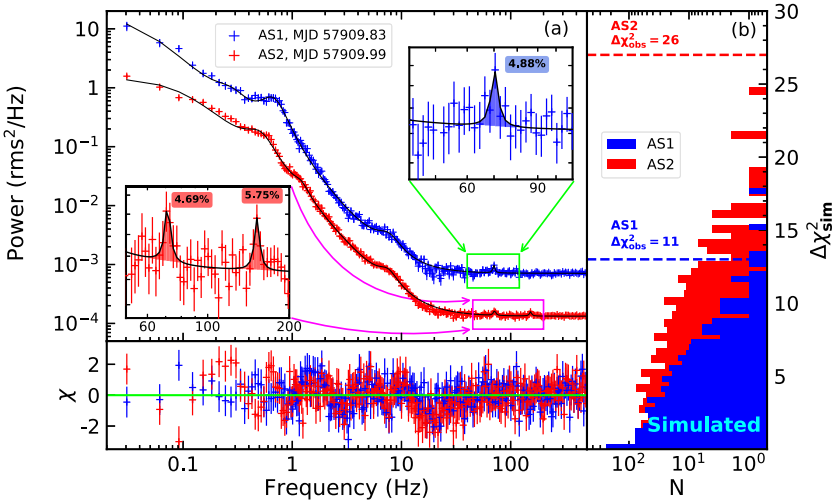



**Figure 5.** Panel (a): Power density spectra of Epoch AS1 and AS2 in the broad-band frequency range (0.01–500 Hz). Each PDS is obtained in 3–60 keV energy band using *LAXPC10* and *LAXPC20* combined observation. Zoomed view of the detected HFQPO and/or harmonic features are shown in the inset. For clarity purpose, PDS of Epoch AS1 is re-scaled by multiplying factor 5. Panel (b): The distribution of $\Delta\chi^2_{sim}$ with the number of occurrences (N), obtained from 1 000 simulated power spectra. The horizontal dash lines denote the $\Delta\chi^2_{obs}$ values obtained using observational date for AS1 (blue) and AS2 (red), respectively. See text for details.

where, $\nu$ is the frequency and $\nu_c$ represents the centroid of the `Lorentzian` profile. Here, $\Delta$ is the full width at half maximum (FWHM) and $K$ is the associated normalisation. We find that multiple `Lorentzian` components at several frequencies are required to fit the PDS continuum over the entire wide-band frequency range. In particular, it is observed that one zero-centroid `Lorentzian` component ($L_0$) along with additional `Lorentzian` components at several distinct frequencies are required to model the red noise continuum. For example, two `Lorentzian` functions $L_1$ and $L_2$ are required to fit the broad bump-like features present at ∼0.65 and ∼7.35 Hz in the power spectra of AS1 (1*b*) observation. In addition, one additional `Lorentzian` component ($L_3$) is needed to fit the power spectral break present at ∼0.25 Hz. It may be noted that the inclusion of each of these additional components ($L_1$-$L_3$) significantly improves the overall fit with a reduction in the fitted $\chi^2$ by ∼29 ($L_1$), 157 ($L_2$), and 28 ($L_3$) for degrees of freedom reduced by 3 corresponding to each component. Interestingly, the significance of these broad features are found to be 12.6$\sigma$ ($L_1$), 10.4$\sigma$ ($L_2$), and 3.2$\sigma$ ($L_3$), whereas the quality factor remains $< 2$, indicating broad characteristics. Note that, we adopt the standard definition of quality factor ($Q = \nu_c/\Delta$) and significance ($\sigma = K/err_{neg}$, where $err_{neg}$ being the negative error in normalisation) in the estimation of the respective quantities following Casella, Belloni, & Stella (2005), Belloni & Altamirano (2013b), Sreehari et al. (2020), Majumder et al. (2022). Similarly, two broad ($Q \lesssim 2$) but significant (∼9$\sigma$) features at ∼0.48 and ∼7.35 Hz are present for AS2 (2*b*). However, unlike AS1 (1*b*), the power spectral break frequency is found to be around ∼1.2 Hz in AS2 (2*b*). As before, modelling of these individual features renders a reduction of $\chi^2$ within 50–275 for 3 degrees of freedom. Moreover, the above findings suggest that these low-frequency broad bump-like features are perhaps connected to inherent variability properties of the 'unknown' class and distinguish it from the other known classes of GRS 1915 + 105.

Interestingly, we observe that significant residuals are still present near ∼70 Hz in both observations (segments 1*b* and 2*b*, see Table 1) which are further modelled using a `Lorentzian` function. The inclusion of additional `Lorentzian` results in a reduction in chi-square ($\chi^2$) of ∼11 (for AS1) with the degrees of freedom (*dof*) reduced by 3. Further, we notice the presence of an additional peak at ∼150 Hz along with ∼70 Hz during the Epoch AS2 (segment 2*b*). As before, simultaneous fitting of both these two peaks reduces $\chi^2$ by ∼26 in AS2. Finally, the best fit of the entire PDS is obtained with $\chi^2/dof$ of 166/228 (segment 1*b* of AS1) and 220/224 (segment 2*b* of AS2). In Figure 5a, we present the best-fitted PDS of Epoch AS1 and AS2, respectively. It is observed that the overall shape of the PDS remain similar for both observations including the broad features present around ∼0.6 Hz and ∼7 Hz, respectively. The residual variations corresponding to the model-fitted PDS are shown in the bottom panel of Figure 5a.

The power spectral modelling indicates the evidence of a HFQPO feature at $70.24^{+0.87}_{-0.85}$ Hz and $71.15^{+1.01}_{-1.05}$ Hz having significance (quality factor) of 2.2$\sigma$ (17.52) and 3$\sigma$ (13.35) in the best fitted PDS of Epoch AS1 (1*b*) and AS2 (2*b*), respectively. In addition, we compute the rms amplitude by taking the square root of the integrated power of the `Lorentzian` function describing the HFQPO feature and find it to be $(4.88 \pm 0.97)$% (AS1) and $(4.69 \pm 0.78)$% (AS2). Further, we also notice the presence of a possible harmonic-like feature at $152.30^{+1.55}_{-2.06}$ Hz (Figure 5) along with the fundamental peak at ∼70 Hz during Epoch AS2. The significance (quality factor) and percentage rms amplitude of the harmonic-like feature are found to be 4.7$\sigma$ (21.07) and $(5.75 \pm 0.81)$%, respectively. In addition, the total rms amplitude over the entire PDS of frequency range 0.01–500 Hz is found to be $(56.33 \pm 10.48)$% and $(57.78 \pm 7.06)$% during Epochs AS1 and AS2, respectively. The best-fitted and estimated HFQPO parameters and the fit statistics for both observations are tabulated in Table 2.

Next, we perform `simftest` (Lotti et al. (2016); Athulya et al. 2022) available within the `XSPEC` environment to further investigate the possible detection of the HFQPO and harmonic features. In general, the `simftest` script[g] simulates synthetic spectra by adding random Poisson noise to the best-fitted model. This

[g]https://heasarc.gsfc.nasa.gov/xanadu/xspec/manual/XspecManual.html.

https://doi.org/10.1017/pasa.2025.10105 Published online by Cambridge University Press

**Table 2.** Details of the detected HFQPO characteristics along with the fit statistics for Epoch AS1 and AS2. Here, $\nu_{\rm HFQPO}$, FWHM, *norm*, *Q-factor*, Sig., and $\rm HFQPO_{rms}$ denote the frequency, width, normalisation, quality factor, significance, and rms amplitude of the detected HFQPO and/or harmonic features. $\rm Total_{rms}$ denotes the rms amplitude of the entire PDS. $\chi^2$/dof indicates the reduced chi-square ($\chi^2_{\rm red}$) of the best fitted PDS. $P_{simftest}$ represents the `simftest` probability. All the errors are computed with 68% confidence level. See text for details.

| Epoch | $\chi^2$/d.o.f | $P_{simftest}$ | $\nu_{\rm HFQPO}$ | FWHM ($\Delta$) | *norm* ($K$) | *Q-factor* | Sig. | $\rm HFQPO_{rms}$ | $\rm Total_{rms}$ |
|---|---|---|---|---|---|---|---|---|---|
| | | ($\times10^{-3}$) | (Hz) | (Hz) | ($\times10^{-4}$) | | ($\sigma$) | (%) | (%) |
| AS1 (1*b*) | 166/228 | 16 | $70.24^{+0.87}_{-0.85}$ | $4.01^{+1.18}_{-1.21}$ | $3.04^{+1.56}_{-1.39}$ | 17.52 | 2.2 | $4.88 \pm 0.97$ | $56.33 \pm 10.48$ |
| AS2 (2*b*) | 220/224 | 1 | $71.15^{+1.01}_{-1.05}$ | $5.33^{+3.32}_{-2.85}$ | $2.34^{+1.05}_{-0.79}$ | 13.35 | 3 | $4.69 \pm 0.78$ | $57.78 \pm 7.06$ |
| | | | $152.30^{+1.55}_{-2.06}$ | $7.23^{+4.25}_{-3.88}$ | $2.59^{+0.73}_{-0.55}$ | 21.07 | 4.7 | $5.75 \pm 0.81$ | $57.78 \pm 7.06$ |

approximates the real statistical fluctuations, expected in the observational data. Next, the fitting is performed for the individual simulated spectra, which allows us to determine the significance of a fitted model component. With this, we generate 1000 simulated power spectra and obtain the simulated $\Delta\chi^2_{\rm sim}$ to compare with the observed $\Delta\chi^2_{\rm obs}$. Here, $\Delta\chi^2_{\rm sim}$ and $\Delta\chi^2_{\rm obs}$ are the change in chi-square statistics with and without fitting the HFQPO and/or harmonic-like feature in the simulated and observed PDS, respectively. The obtained results are depicted in Figure 5b using histogram. We find that for both AS1 and AS2, $\Delta\chi^2_{\rm obs}$ resides away from the main simulated distribution of $\Delta\chi^2_{\rm sim}$. These findings yield a 'low' chance probability of ∼0.001 and 0.016 of getting the features by random statistical fluctuations in AS1 and AS2, respectively. Moreover, based on these statistical analyses and the best-fitted HFQPO parameters (see Table 2), we conclude the possible evidence of HFQPO and/or harmonic features in AS1 and AS2 observations, respectively. However, low significance of the observed features (see Table 2) possibly implies the feeble nature of the HFQPOs and therefore the results should be interpreted accordingly. It is worth mentioning that the PDS for all the segments of AS1 and AS2 along with rest of the observations in Table 1 are analysed. However, we find the presence of HFQPOs for the segments 1*b* and 2*b* only, and therefore, the results are presented in Figure 5 and Table 2 for these observation segments.

Further, we examine the power spectral properties of $\chi_3$, κ, and μ classes using *RXTE/PCA* data and compare with that of the 'unknown' variability class observed during AS1 and AS2. The PDS computation is performed following the similar methodology described above and modelled using the combination of `constant` and `Lorentzian` components. In Figure 6, we present the PDS corresponding to $\chi_3$, κ, and μ classes in 2–60 keV energy band. We observe that a strong low-frequency QPO is present at ∼5 Hz in the PDS of $\chi_3$ class, whereas broad bump-like features are visible around ∼6 Hz in the κ and μ class observations. In addition, a QPO-like feature seems to be present at ∼3 Hz in the PDS of κ class. Moreover, it is evident that the overall shape of the PDS in μ and κ class including the low-frequency power spectral break near ∼0.1 and ∼0.6 Hz along with bump-like features around ∼6 Hz remain marginal identical to the PDS obtained during AS1 and AS2 (see Figure 5) without the presence of HFQPOs. However, the appearance of a strong QPO feature at ∼5 Hz along with a flat-topped noise distribution at lower frequencies makes the PDS of $\chi_3$ observation completely distinct from the rest of the classes.

### 3.5. On the modelling of LFQPO

In this section, we examine the accuracy in modelling the low-frequency (< 20 Hz) domain of the PDS. In doing so, we consider

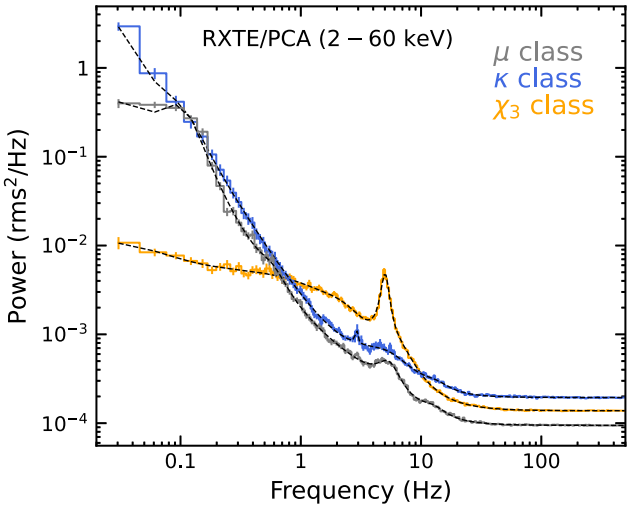



**Figure 6.** The PDS in 2–60 keV energy band of $\chi_3$, κ, and μ classes corresponding to the same observations for which the light curves are presented in Figures 4. See text for details.

the PDS of the AS1 observation up to 20 Hz for modelling, which is shown in the top panel of Figure 7. The bottom panels of Figure 7 present the variation of model fitted residuals with different model combinations as described below. First, we fit one simple `powerlaw` to model the red noise part of the PDS and obtain a reduced chi-square ($\chi^2_{\rm red}$) of 7 with large variations in the residuals. Next, we include one `Lorentzian` (L1) component at 0.6 Hz to fit the LFQPO-like feature. This yields a worst fit for a $\chi^2_{\rm red} = 3.6$ with significant residual variation at 0.2–0.3 Hz and 7–8 Hz (see Figure 7). Hence, we include two additional `Lorentzian` components (L2 and L3) to model these bump-like features, resulting in a $\chi^2_{\rm red} = 0.9$ (see Figure 7). Moreover, we note that excluding either the L2 or L3 component from the fit results in $\chi^2_{\rm red}$ value exceeding 1.3. From this modelling, we find the significance of the broad LFQPO-like feature at 0.63 Hz to be around $11.2\sigma$. Note that the broadband (0.01–500 Hz) PDS modelling (see Section 3.4) resulted in the centroid frequency and significance of this feature as 0.65 Hz and $12.6\sigma$, respectively. This suggests that the characteristic frequency of the LFQPO-like feature and its properties remain independent of the choice of modelling the red noise component. Furthermore, a careful investigation of the model-fitted PDS in Figure 7 indicates that the `powerlaw` dominates in the modelling of the red noise component only below ∼0.18 Hz. On the other hand, the presence of two broad bump-like features at ∼0.2 and ∼7 Hz dominates over `powerlaw` in modelling the overall red noise variation. This further suggests that the red noise in the PDS deviates significantly

https://doi.org/10.1017/pasa.2025.10105 Published online by Cambridge University Press

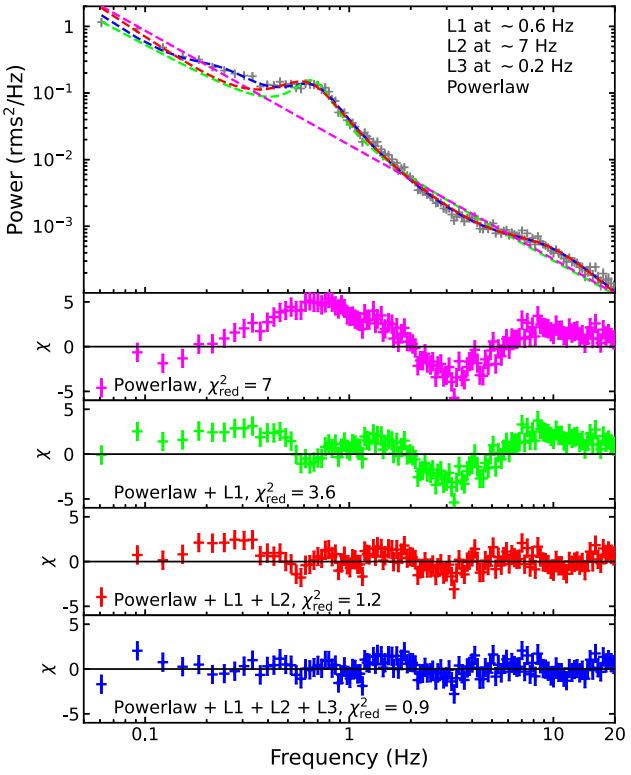



**Figure 7.** *Top panel:* PDS of the AS1 observation up to 20 Hz, highlighting the low-frequency variability properties. Dashed lines in different colours represent the model combinations used in the PDS modelling. *Bottom panels:* Variation of the model-fitted residuals for different model combinations, as indicated in the figure. See text for details.

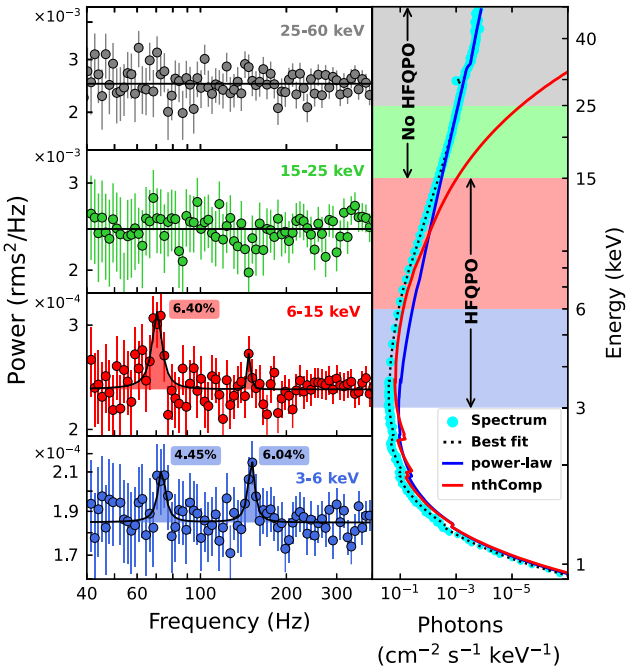



**Figure 8.** *Left panel*: Energy dependent power density spectra of Epoch AS2. In top to bottom panels, the best fitted PDS in different energy ranges are depicted. *Right panel*: Best fitted wide-band (0.7–50 keV) energy spectrum of combined *SXT* and *LAXPC* observations. The dotted (black) and solid curves (blue/red) represent the best fitted models and spectral components used in the modelling. The shaded regions with different colours represent the energy bands for which the PDS are computed. See text for details.

from a simple `powerlaw` form and needs to be modelled using multiple `Lorentzian` components at distinct frequencies, as also demonstrated in Section 3.4 during the broadband PDS modelling.

### 3.6. Energy dependent power spectra

We intend to study the energy-dependent properties of the possible HFQPO and harmonic features obtained in the preceding section. Accordingly, we generate PDS in 3–6, 6–15, 15–25, and 25–60 keV energy bands and present the obtained results for AS2 in Figure 8 (left panel). To ascertain the signature of HFQPO and/or harmonic-like features, we fit `Lorentzian` components at the respective frequencies (Table 2) and compute significance ($\sigma$) and rms amplitudes (in per cent). We find that in 3–6 keV energy band, a weak feature of HFQPO at ~70 Hz is present with significance ~1.8$\sigma$ and rms ~4.45%. However, the possible harmonic at ~150 Hz is seen to be more prominent with a significance of ~4.3$\sigma$ and rms ~6.04%. On the contrary, in 6–15 keV energy band, the evidence of HFQPO is seen to be more prominent with a significance of ~3.2$\sigma$ and rms ~6.43%, whereas the harmonic-like feature appears to be insignificant. Moreover, the PDS remains featureless in 15–25 and 25–60 keV energy bands, respectively. In Figure 8 (right panel), we present the best-fitted energy spectrum (more details in Section 4) of the source from combined *SXT* and *LAXPC* data in 0.7–50 keV energy band. The model components used in the spectral modelling are indicated at the inset in different colours (`nthcomp` in red and `powerlaw` in blue). We observe that the contribution of the Comptonized component (`nthcomp`) remains significant till ~15 keV, where the evidence of HFQPO and/or harmonic features are observed. This suggests that Comptonized emissions are perhaps attributed to these features.

## 4. Spectral analysis and results

We generate energy spectra of the two selected observations (AS1 and AS2) in the wide-band energy range of 0.7–50 keV by combining both *SXT* and *LAXPC* spectra. The *SXT* spectra are obtained considering 0.7–7 keV energy range. We use *LAXPC20* spectra in 3–50 keV energy range which are extracted using `LaxpcSoftv3.4.4`[h] (Antia et al. 2017). We follow the standard procedure to use the background, response, and ancilliary files of *SXT* and *LAXPC* for spectral modelling (see Majumder et al. 2022, for details). Each of the combined spectra from *SXT* and *LAXPC* is modelled using `XSPEC V12.13.1` in `HEASOFT V6.32.1` to understand the spectral properties of the source. During spectral fitting, we use the `gain fit` command to adjust the low energy residuals at 1.8 and 2.2 keV observed in *SXT* spectra. Following Antia et al. (2017), a systematic error of 2% is incorporated during spectral fitting (Leahy & Chen 2019; Sreehari et al. 2020; Majumder et al. 2022).

We adopt the physically motivated model combination comprising of a thermal Comptonization component (`nthcomp`) Zdziarski et al. (1996) and a `powerlaw` component to fit the wide-band spectra in 0.7–50 keV energy range. The inter-galactic absorption is taken care by including `Tbabs` (Wilms, Allen, & McCray 2000) in the spectral modelling. Following Majumder

[h] http://www.tifr.res.in/astrosat_laxpc/LaxpcSoft.html.

https://doi.org/10.1017/pasa.2025.10105 Published online by Cambridge University Press

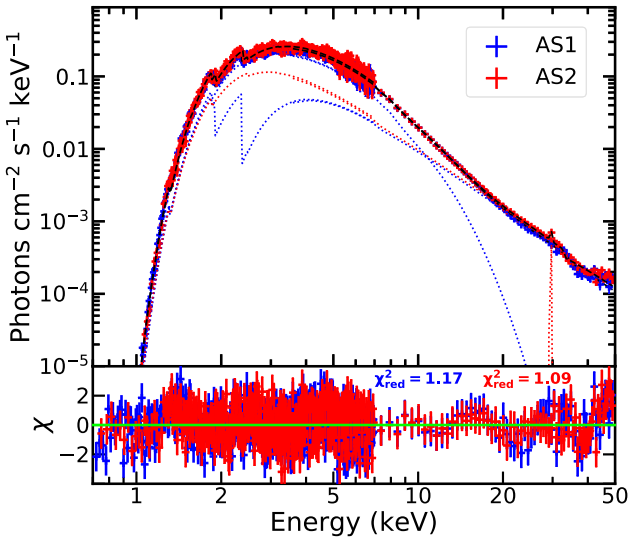



**Figure 9.** Best-fitted unfolded wide-band (0.7–50 keV) energy spectra of GRS 1915 + 105 during Epochs AS1 and AS2. The spectra are modelled with `(Tbabs)` × `smedge` × `(nthComp + powerlaw)` × `constant`. The bottom panel shows the variation of residuals in units of $\sigma$. See text for details.

et al. (2022), a `constant` component is included in the spectral fitting to adjust the cross-calibration of the data from *SXT* and *LAXPC* instruments. During the entire spectral analysis, we keep the column density fixed at $6 \times 10^{22}$ atoms/cm$^2$ (Yadav et al. 2016; Sreehari et al. 2020; Majumder et al. 2022). We find that the above model prescription is inadequate to fit the wide-band spectra of both observations (AS1 and AS2) with significant residual left near ∼9 keV. Hence, we include a `smedge` component to adjust the residuals left at ∼9 keV. Accordingly, the final model combination, namely `(Tbabs)` × `(smedge)` × `(nthComp)` + `(powerlaw)` × `constant` is found to provide the best description of all the observed spectra with a reasonable reduced chi-square value ($\chi^2_{red} = \chi^2/dof$) of 1.17 (AS1) and 1.09 (AS2). We note that a `gaussian` is needed to fit the 'bump' present near ∼30 keV in the *LAXPC* spectra (Antia et al. 2021; Aneesha et al. 2024) of AS2. In Figure 9, we present the best fitted energy spectra of AS1 and AS2 along with residuals using different colours.

The best fitted spectral parameters for observation AS1 (AS2) are obtained as `nthcomp` photon index $\Gamma_{nth} = 1.96^{+0.05}_{-0.02}$ ($1.94^{+0.08}_{-0.06}$), electron temperature $kT_e = 1.71^{+0.09}_{-0.04}$ ($1.65^{+0.09}_{-0.07}$) keV and power-law photon index $\Gamma_{PL} = 2.78^{+0.04}_{-0.03}$ ($2.75^{+0.03}_{-0.02}$), respectively. Note that the seed photon temperature of `nthcomp` remains unconstrained during the fitting, hence we keep it fixed at 0.2 keV. We estimate the bolometric flux in 1–100 keV energy range using the convolution model `cflux`, keeping the model normalisation fixed at the best fitted values. The corresponding bolometric luminosity ($L_{bol}$) is found to be $L_{bol} \sim 0.42\, L_{Edd}$ for both observations, where $L_{Edd}$ refers to the Eddington luminosity. This indicates that the source was in the sub-Eddington accretion regime during Epoch AS1 and AS2, respectively. Further, following Zdziarski et al. (1996) and using the model fitted spectral parameters, we compute the optical depth as ∼13.94 (AS1) and ∼14.42 (AS2), and Compton y-parameter as ∼2.61 (AS1) and ∼2.68 (AS2). This implies the presence of an optically thick Comptonizing corona responsible for the non-thermal emission in the spectra.

## 5. Discussion

In this paper, we carry out comprehensive analyses of two GT observations of GRS 1915+105 during June 2017 with *AstroSat* to examine the variability properties of the source. The obtained findings from the detailed spectro-temporal studies are discussed below.

### 5.1. An 'unknown' variability class in GRS 1915+105

The light curves during Epoch AS1 show the presence of aperiodic 'dips' of few tens of seconds duration along with the 'flare' like features immediately after the 'dip' (Figure 2a). The variation of HR also exhibits the signature of the 'dip' segments. In the CCD of Epoch AS1, we observe a uniform '*C*' shaped distribution with two elongated branches extended towards the higher HR1 and HR2 domains. Interestingly, the 'dip' and 'flare' like features in the light curve along with elongated branches in the CCD are not seen in Epoch AS2 (Figure 2c and Table 1).

Upon comparing with the existing variability classes observed with *AstroSat*, we confirm that this 'unknown' class is 'softer' (Majumder et al. 2022) in nature as HR1 ∼ 0.62 and HR2 ∼ 0.04. The short duration and aperiodic 'dips'/'flares' including the CCD features seem to be different from the λ, ω, and κ classes (Belloni et al. 2000); Athulya et al. 2022). Further, it is noted that the typical duration of each beat in the canonical ρ class variability of the heartbeat state is about ∼60–70 s and the hardness ratios ($0.5 \lesssim$ HR1 $\lesssim 0.8$ and $0.05 \lesssim$ HR2 $\lesssim 0.2$) indicate towards harder variability properties. Therefore, the 'flare' like features (of duration ∼40–50 s) in the light curve of AS1 and the corresponding CCD variation appear to be marginally similar to the canonical ρ class. Moreover, in Epoch AS0, 16 days prior to AS1, the source exhibits ρ class (Figure 2e, Table 1). During Epoch AS3, after 33 days of AS2, the source displays κ class variability (Figure 2e). We also notice that the combined CCD of ρ and κ class observations marginally overlap with that of AS1.

Meanwhile, several studies are carried out to explain the origin of ρ class variability in GRS 1915 + 105, relying on the classical disc instability model (Lightman & Eardley 1974) for a truncated accretion disc and compact corona configuration (Honma et al. 1991; Taam et al. 1997; Szuszkiewicz & Miller 1998; Janiuk, Czerny, & Siemiginowska 2000). Further, Massa et al. (2013) argued that the limit cycle behaviour, which mostly depends on the accretion rate, is typical for the ρ class variability and explains the hard lags as well. Moreover, Nandi et al. (2000) proposed that the bursts in the light curve of ρ class are closely associated with the so-called 'On' state of the source. Most importantly, they found the features of the small-scaled version of a structured ρ class in the light curve of canonical κ class variability. This essentially indicates the intrinsic connection between these variability signatures, perhaps produced from the interplay of inner Comptonizing corona and the feedback of disc winds (Nandi et al. 2000; Chakrabarti & Nandi 2000). A phenomenological non-linear mathematical model has also been put forward to describe the complex variability classes of GRS 1915 + 105 (Massaro et al. 2020a, b). This model contains an input function $J(t)$ which is used to reproduce light curves of various classes. For example, constant input values (Massaro et al. 2020a) reproduce the classes χ, δ, and ρ, while several other classes (α, γ, λ, κ, ω, ξ, and θ) result when rather simple step function or sawtooth modulations of $J(t)$ are considered (Massaro et al. 2020b). We find that the model with a constant input function is unable to reproduce the structured variability signatures

https://doi.org/10.1017/pasa.2025.10105 Published online by Cambridge University Press

consisting of irregular low-count dips and spike-like features as observed in the light curve of the 'unknown' variability class ($\tau$). These findings further suggest that the class $\tau$ is quite different from the canonical $\chi$ and $\rho$ classes and possibly could not be explained as a transition between these two classes. However, we cannot exclude the possibility of getting a functional form of $J(t)$, which could model the $\tau$ class variability. It is noteworthy that Alberti et al. (2022) also proposed a formalism based on a stochastic dynamical process to describe the complex variability signatures of GRS 1915 + 105. However, applying such models to the present data is beyond the scope of this work and will be addressed elsewhere.

However, the detection of $\delta$ class variability from *NuSTAR* observation (Figure 2e) within 18 days of AS2 suggests that the observed variability is not just a combined feature of $\rho$ and $\kappa$ classes during $\rho \rightarrow \kappa$ transition, instead it resembles more complex variability signature. Additionally, in Epoch AS1 and AS2, we observe distinct characteristics, such as low-frequency breaks at ∼0.6 and ∼7 Hz in the wide-band (0.01–500 Hz) PDS (see Figure 5) as compared to the known 'softer' variability classes (Majumder et al. 2022). Considering all these findings, we infer that the variability patterns seen in the light curves of Epochs AS1 and AS2 perhaps correspond to an 'unknown' variability class compared to the previously reported 15 known classes of GRS 1915 + 105.

### 5.2. Possible detection of twin peak HFQPO

The power spectral analysis indicates the evidence of possible HFQPO features at frequencies ∼70 and 71 Hz (Figure 5) with rms of $(4.88 \pm 0.97)\%$ and $(4.69 \pm 0.78)\%$ for Epochs AS1 and AS2, respectively (Table 2). Moreover, in Epoch AS2, we find the presence of a harmonic-like feature at ∼152 Hz with rms of $(5.75 \pm 0.81)\%$ (see Figure 5 and Table 2). Indeed, for GRS 1915+105, the well known HFQPO at ∼70 Hz is already reported with *RXTE* (Belloni & Altamirano 2013b) and *AstroSat* (Majumder et al. 2022, and reference therein). A broad QPO feature of weak coherence (Q ∼ 2) at 170 Hz is also reported during the hard intervals of $\theta$ class with *RXTE* (Belloni et al. 2006). Interestingly, an additional feature of frequency 27–41 Hz (Belloni, Méndez, & Sánchez-Fernández 2001; Strohmayer 2001b) and twin peak HFQPO feature at 34 and 68 Hz (Belloni & Altamirano 2013a) are also found from *RXTE* observations. It is noteworthy that twin peak HFQPOs are confirmed in a few other BH-XRBs, such as GRO J1655−40 (Remillard et al. 1999; Remillard et al. 2002), XTE J1550−564 (Remillard et al. 2002), and IGR J17091−3624 (Altamirano & Belloni 2012).

The study of energy dependent PDS in Epoch AS2 indicates that the possible HFQPO feature at ∼70 Hz is present in 3–15 keV energy range, whereas the harmonic-like feature only seems to appear in 3–6 keV. We observe that the strength of the HFQPO feature is more (rms ∼6.43%) in 6–15 keV energy band as compared to 3–6 keV band (rms ∼4.45%). These findings are coarsely in agreement with the results of Majumder et al. (2022), except a weak signature of HFQPO present below $\lesssim$ 6 keV.

### 5.3. Connection of HFQPOs with spectral features

The wide-band (0.7–50 keV) energy spectra of *SXT* and *LAXPC* are well described by the model consisting of a thermal Comptonisation component (`nthcomp` in `XSPEC`) and an additional `powerlaw` component (see Section 4). The best-fitted spectra of Epoch AS1 (AS2) yields an electron temperature $kT_e \sim 1.71(1.65)$ keV, `nthcomp` photon index $\Gamma_{\rm nth} \sim 1.96(1.94)$, and a steep `powerlaw` photon index $\Gamma_{\rm PL} \sim 2.78(2.75)$. The source is found to remain in the sub-Eddington regime with bolometric luminosity $L_{\rm bol} \sim 42\%\ L_{\rm Edd}$ during Epochs AS1 and AS2 (see Section 4). We estimate the optical depth and Compton y-parameter as ∼14 and ∼3 for both observations. This indicates the presence of an optically thick corona responsible for the generation of high energy continuum in the wide-band spectra. Evidently, the requirement of an additional `powerlaw` component with a steeper index (∼2.8) corroborates the presence of an extended corona along with the compact 'Comptonizing corona' (Sreehari et al. 2020; Majumder et al. 2022).

Most importantly, the evidence of possible HFQPO and its harmonic-like feature are found in the energy range ($\lesssim$ 15 keV), where Comptonized component dominates in the energy spectra (see Figure 8). This possibly implies that only the Comptonized photons within 3–15 keV energy range participate in such oscillations. Meanwhile, several theoretical studies of accretion dynamics around black holes attempt to explain the HFQPOs observed in various BH-XRBs including GRO J1655 − 40, GRS 1915 + 105, XTE J1550 − 564, and H 1743 − 322 from the modulation of the boundary of Comptonizing region (Aktar et al. 2017, 2018; Dihingia et al. 2019). Moreover, comprehensive spectro-temporal correlation studies of GRS 1915 + 105 in the presence of HFQPOs reveal the inherent connection between the origin of these features and the Comptonized emission seen in the energy spectra of four distinct variability classes (Sreehari et al. 2020; Majumder et al. 2022). Considering all these and based on the present findings, we speculate that the oscillation of the 'Comptonizing corona' seems to play a viable role in exhibiting the possible HFQPOs observed in an 'unknown' variability class of GRS 1915 + 105.

## 6. Conclusions

In this paper, we perform detailed spectro-temporal analyses of GRS 1915 + 105 using *AstroSat* observations during June, 2017. We observe that the source undergoes a transition from $\rho$ to $\kappa$ class and during such transition, the source displays an 'unknown' variability class ($\tau$) of GRS 1915 + 105, where irregular repetition of low count 'dips' along with 'flare' like features are observed between the successive steady light curve variations. Note that the source exhibits $\delta$ class variability before transiting to $\kappa$ class, therefore, we ascertain that the 'unknown' ($\tau$) type variability is possibly different from the existing 15 variability classes of GRS 1915+105. In addition, we find the evidence of possible HFQPO feature at ∼71 Hz along with a harmonic-like signature at ∼152 Hz. Finally, the wide-band spectral results indicate the presence of a 'Compact corona' surrounding the source, which seems to regulate the observed HFQPO features in GRS 1915 + 105.

**Acknowledgements.** Authors thank the anonymous reviewer for constructive comments and useful suggestions that helped to improve the quality of the manuscript. AN thanks Group Head (Space Astronomy Group – SAG), Deputy Director (Payload, Data Management & Space Astronomy Area – PDMSA), and the Director (U R Rao Satellite Centre – URSC) for encouragement and continuous support to carry out this research. This publication uses the data from the *AstroSat* mission of the Indian Space Research Organisation (ISRO), archived at the Indian Space Science Data Centre (ISSDC). This work has used the data from the Soft X-ray Telescope (SXT) developed at TIFR, Mumbai, and the SXT-POC at TIFR is thanked for verifying and releasing the data and providing the necessary software tools. This work has also used

the data from the *LAXPC* Instruments developed at TIFR, Mumbai, and the LAXPC-POC at TIFR is thanked for verifying and releasing the data. We also thank the *AstroSat* Science Support Cell hosted by IUCAA and TIFR for providing the `LAXPCSOFT` software which we used for *LAXPC* data analysis. The authors thank *NuSTAR* and *RXTE* instrument teams for processing the data and providing the necessary software for analysis.

**Data availability statement.** *AstroSat* data used for this publication are currently available at the Astrobrowse (AstroSat archive) website (https://astrobrowse.issdc.gov.in/astro_archive/archive) of the Indian Space Science Data Center (ISSDC). The *NuSTAR* and *RXTE* data used in this work are archived at the HEASARC data center (https://heasarc.gsfc.nasa.gov/db-perl/W3Browse/w3browse.pl).

## References

Agrawal, P. C. 2006, AdSR, 38, 2989
Agrawal, P. C., et al. 2017, JApA, 38, 30
Agrawal, V. K., Nandi, A., Girish, V., & Ramadevi, M. C. 2018, MNRAS, 477, 5437
Aktar, R., Das, S., Nandi, A., & Sreehari, H. 2017, MNRAS, 471, 4806
Aktar, R., Das, S., Nandi, A., & Sreehari, H. 2018, JApA, 39, 17
Alberti, T., Massaro, E., Mineo, T., & Feroci, M. 2022, MNRAS, 517, 3568
Altamirano, D., & Belloni, T. 2012, ApJ, 747, L4
Aneesha, U., Das, S., Katoch, T. B., & Nandi, A. 2024, MNRAS, 532, 4486
Antia, H. M., et al. 2017, ApJS, 231, 10
Antia, H. M., et al. 2021, JApA, 42, 32
Athulya, M. P., & Nandi, A. 2023, MNRAS, 525, 489
Athulya, M. P., et al. 2022, MNRAS, 510, 3019
Balakrishnan, M., et al. 2021, ApJ, 909, 41
Belloni, T., Klein-Wolt, M., Méndez, M., van der Klis, M., & van Paradijs, J. 2000, A&A, 355, 271
Belloni, T., Méndez, M., & Sánchez-Fernández, C. 2001, A&A, 372, 551
Belloni, T., Soleri, P., Casella, P., Méndez, M., & Migliari, S. 2006, MNRAS, 369, 305
Belloni, T. M., & Altamirano, D. 2013a, MNRAS, 432, 19
Belloni, T. M., & Altamirano, D. 2013b, MNRAS, 432, 10
Beri, A., et al. 2019, MNRAS, 482, 4397
Casella, P., Belloni, T., & Stella, L. 2005, ApJ, 629, 403
Castro-Tirado, A. J., Brandt, S., & Lund, N. 1992, IAU, 5590
Chakrabarti, S. K., & Nandi, A. 2000, arXiv e-prints, astro
Chakrabarti, S. K., Nandi, A., Chatterjee, A. K., Choudhury, A. K., & Chatterjee, U. 2005, A&A, 431, 825
Chakrabarti, S. K., Nandi, A., Choudhury, A., & Chatterjee, U. 2004, ApJ, 607, 406
Dihingia, I. K., Das, S., Maity, D., & Nandi, A. 2019, MNRAS, 488, 2412
Greiner, J., Morgan, E. H., & Remillard, R. A. 1996, ApJ, 473, L107
Hannikainen, D. C., et al. 2005, A&A, 435, 995
Harikesh, S., Majumder, S., Das, S., & Nandi, A. 2025, MNRAS, 540, 2965
Honma, F., Matsumoto, R., Kato, S., & Abramowicz, M. A. 1991, PASJ, 43, 261
Janiuk, A., Czerny, B., & Siemiginowska, A. 2000, ApJ, 542, L33
Janiuk, A., Czerny, B., & Siemiginowska, A. 2002, ApJ, 576, 908
Klein-Wolt, M., et al. 2002, MNRAS, 331, 745
Leahy, D. A., & Chen, Y. 2019, ApJ, 871, 152
Leahy, D. A., et al. 1983, ApJ, 266, 160
Lightman, A. P., & Eardley, D. M. 1974, ApJ, 187, L1
Lotti, S., et al. 2016, ApJ, 822, 57
Majumder, P., Dutta, B. G., & Nandi, A. 2024, MNRAS, 527, 4739
Majumder, P., Dutta, B. G., & Nandi, A. 2025, MNRAS, 540, 37
Majumder, S., et al. 2022, MNRAS, 512, 2508
Massa, F., et al. 2013, A&A, 556, A84
Massaro, E., et al. 2020a, MNRAS, 495, 1110
Massaro, E., et al. 2020b, MNRAS, 496, 1697
Méndez, M., Altamirano, D., Belloni, T., & Sanna, A. 2013, MNRAS, 435, 2132
Morgan, E. H., Remillard, R., Muno, M., & Kitzgibbons, K. 1999, in AAS/High Energy Astrophysics Division, Vol. 4, AAS/High Energy Astrophysics Division #4, 28.11
Motta, S. E., et al. 2021, MNRAS, 503, 152
Muno, M. P., Morgan, E. H., & Remillard, R. A. 1999, arXiv e-prints, astro
Naik, S., Agrawal, P. C., Rao, A. R., & Paul, B. 2002, MNRAS, 330, 487
Nandi, A., Debnath, D., Mandal, S., & Chakrabarti, S. K. 2012, A&A, 542, A56
Nandi, A., Manickam, S. G., & Chakrabarti, S. K. 2000, arXiv e-prints, astro
Nandi, A., Manickam, S. G., Rao, A. R., & Chakrabarti, S. K. 2001, MNRAS, 324, 267
Nathan, E., et al. 2022, MNRAS, 511, 255
Neilsen, J., Remillard, R. A., & Lee, J. C. 2011, ApJ, 737, 69
Pahari, M., & Pal, S. 2009, arXiv e-prints, arXiv:0906.4611
Parrinello, K., et al. 2023, in American Astronomical Society Meeting Abstracts, Vol. 55, American Astronomical Society Meeting Abstracts, 469.01
Paul, B., et al. 1997, A&A, 320, L37
Paul, B., et al. 1998a, in The Hot Universe, Vol. 188, ed. K. Koyama, S. Kitamoto, & M. Itoh, 394
Paul, B., et al. 1998b, A&AS, 128, 145
Paul, B., et al. 1998c, ApJ, 492, L63
Rawat, D., et al. 2019, ApJ, 870, 4
Remillard, R. A., McClintock, J. E., Orosz, J. A., & Levine, A. M. 2006, ApJ, 637, 1002
Remillard, R. A., Morgan, E. H., McClintock, J. E., Bailyn, C. D., & Orosz, J. A. 1999, ApJ, 522, 397
Remillard, R. A., Muno, M. P., McClintock, J. E., & Orosz, J. A. 2002, ApJ, 580, 1030
Rodriguez, J., et al. 2004, ApJ, 615, 416
Singh, K. P., et al. 2014, in Society of Photo-Optical Instrumentation Engineers (SPIE) Conference Series, Vol. 9144, Space Telescopes and Instrumentation 2014: Ultraviolet to Gamma Ray, ed. T. Takahashi, J.-W. A. den Herder, & M. Bautz, 91441S
Singh, K. P., et al. 2016, in Society of Photo-Optical Instrumentation Engineers (SPIE) Conference Series, Vol. 9905, Space Telescopes and Instrumentation 2016: Ultraviolet to Gamma Ray, ed. J.-W. A. den Herder, T. Takahashi, & M. Bautz, 99051E
Singh, K. P., et al. 2017, JApA, 38, 29
Sreehari, H., et al. 2020, MNRAS, 499, 5891
Sreehari, H., et al. 2019, MNRAS, 487, 928
Strohmayer, T. E. 2001a, ApJ, 552, L49
Strohmayer, T. E. 2001b, ApJ, 554, L169
Szuszkiewicz, E., & Miller, J. C. 1998, MNRAS, 298, 888
Taam, R. E., Chen, X., & Swank, J. H. 1997, ApJ, 485, L83
Uttley, P., Cackett, E. M., Fabian, A. C., Kara, E., & Wilkins, D. R. 2014, A&A Rev., 22, 72
van der Klis, M. 1988, in NATO Advanced Science Institutes (ASI) Series C, Vol. 262, NATO Advanced Science Institutes (ASI) Series C, ed. H. Ögelman & E. P. J. van den Heuvel (Dordrecht: Kluwer Academic Publishers), 27
Vaughan, S., Edelson, R., Warwick, R. S., & Uttley, P. 2003, MNRAS, 345, 1271
Vilhu, O., & Nevalainen, J. 1998, ApJ, 508, L85
Weng, S.-S., Wang, T.-T., Cai, J.-P., Yuan, Q.-R., & Gu, W.-M. 2018, ApJ, 865, 19
Wilms, J., Allen, A., & McCray, R. 2000, ApJ, 542, 914
Yadav, J. S., et al. 1999, ApJ, 517, 935
Yadav, J. S., et al. 2016, in Society of Photo-Optical Instrumentation Engineers (SPIE) Conference Series, Vol. 9905, Space Telescopes and Instrumentation 2016: Ultraviolet to Gamma Ray, ed. J.-W. A. den Herder, T. Takahashi, & M. Bautz, 99051D
Zdziarski, A. A., Johnson, W. N., & Magdziarz, P. 1996, MNRAS, 283, 193
Zhang, W., Jahoda, K., Swank, J. H., Morgan, E. H., & Giles, A. B. 1995, ApJ, 449, 930
Zhang, Y., et al. 2022, MNRAS, 514, 2891

https://doi.org/10.1017/pasa.2025.10105 Published online by Cambridge University Press